PROCEEDINGS OF SCIENCE

Scintillating light track reconstruction for fast neutron detection based on deep learning techniques

Samuele Lanzi,[a,*] **Patrizio Console Camprini,**[b] **Francesco Giacomini,**[c] **Cristian Massimi,**[a,b] **Alberto Mengarelli,**[b] **Licia Mozzina,**[a] **Claudia Pisanti,**[a] **Riccardo Ridolfi,**[a] **Roberto Spighi**[b] **and Mauro Villa**[a]

[a] *Department of Physics and Astronomy, University of Bologna*
Viale Berti Pichat 6/2, Bologna, Italy
[b] *Istituto Nazionale di Fisica Nucleare (INFN),*
Viale Berti Pichat 6/2, Bologna, Italy
[c] *INFN-CNAF,*
Viale Berti Pichat 6/2, Bologna, Italy

E-mail: samuele.lanzi2@unibo.it

Imaging techniques based on tracking have progressed from manual examination to the utilization of contemporary photodetectors, like SiPM arrays and CMOS cameras, to convert scintillation light into digital data and obtain physical information. This study presents RIPTIDE, a novel recoil-proton track imaging system designed for fast neutron detection, with an emphasis on the use of deep-learning methods. RIPTIDE utilizes neutron-proton elastic scattering within a plastic scintillator to produce scintillation light, creating images that document scattering occurrences. A deep neural network is employed to rectify optical distortions in proton track images, enhancing their form and alignment. This adjustment improves the precision of track length measurements, which directly affects proton energy estimation and neutron kinematics reconstruction.

International Symposium on Grids and Clouds (ISGC2025)
16 -21 March 2025
Academia Sinica Grid Computing Centre (ASGC), Taipei, Taiwan

*Speaker

 ISSN 1824-8039 . Published by SISSA Medialab.

PoS(ISGC2025)021

Contents

1. Introduction

Progress in neutron detector technology has been closely linked to developments of particle detector instrumentation, as both fields share cutting-edge technological foundations. Nevertheless, while charged particle tracking is a well-established technique, neutron tracking systems remain under development. Currently, only a limited number of detector concepts or feasibility studies are documented in the literature, as seen in [1–5]. The reconstruction of fast neutron momentum requires precise tracking of detected neutrons [6]. In this context, two-particle reactions offer significant advantages, with neutron-proton (n-p) elastic scattering representing the most straightforward interaction mechanism.

State-of-the-art neutron tracking techniques based on single and double n-p scattering have been developed by the SONTRAC [7] and MONDO [2, 9] collaborations. Both systems rely on multiple n-p scattering events: SONTRAC is designed for solar MeV-neutron detection in space missions, while MONDO targets fast neutrons produced in particle therapy treatments. These detectors employ a matrix of plastic scintillating fibers to track recoiling protons. The resulting scintillation light is then amplified either by an image intensifier in MONDO or read out via silicon photomultipliers in SONTRAC. The primary challenges of these pioneering systems include channel readout, data transfer efficiency, and detection threshold limitations.

To address these limitations, our group recently proposed a novel detector concept called RIPTIDE (RecoIl Proton Track Imaging DEtector) [10–13]. This system consists of a monolithic plastic scintillator coupled to a lens system and a readout system (see Figure 1). The key innovation lies in using the scintillator light output to achieve full spatio-temporal reconstruction of n-p

scattering events. By stereoscopically imaging recoil-proton tracks, the apparatus enables neutron spectrometry and real-time analysis of energy deposition along charged particle trajectories. In essence, RIPTIDE exploits the same physical interaction as SONTRAC and MONDO but is designed to have more spatial resoluton.

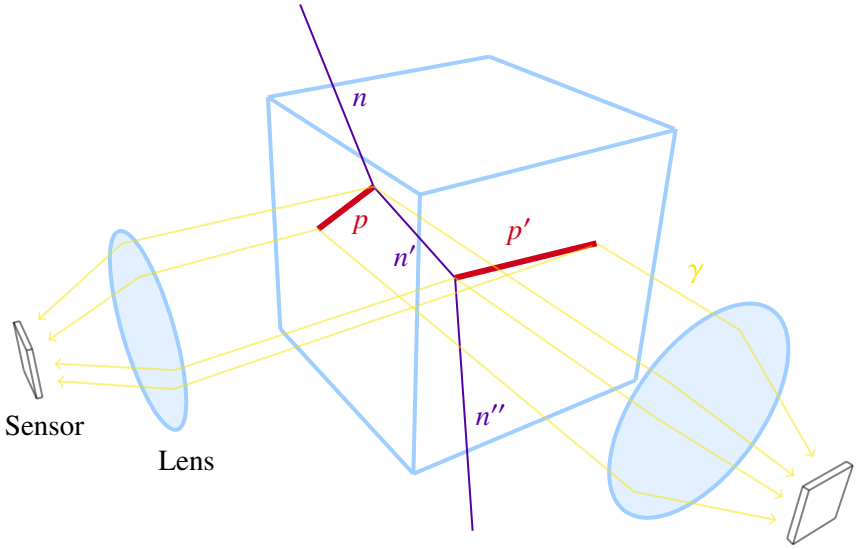

Figure 1: *The RIPTIDE detector concept.*

This work presents an analysis of the detector operation, covering neutron-proton scattering kinematics as well as image processing and analysis techniques. We describe the Geant4 simulation framework used to model neutron interactions and optical photon transport within the plastic scintillator. The track reconstruction method combines traditional computer vision techniques with deep learning. Our results demonstrate accurate 3D track reconstruction, enabling neutron energy determination.

2. Proton recoil technique and neutron tracking in RIPTIDE

The basic tool for full neutron momentum reconstruction in Recoil Proton Track Imaging (RPTI) detectors is two-body kinematics, where the neutron energy E_n is related to the proton recoil angle and energy (θ_p, E_p) by the relationship:

$$E_n = \frac{E_p}{\cos^2 \theta_p}. \tag{1}$$

When the neutron source position is known, this technique enables neutron energy determination through observation of a single neutron-proton scattering event (Figure 2a). In cases where the neutron undergoes two consecutive interactions with protons known as double scattering (Figure 2b) both the neutron energy and direction can be fully reconstructed. By connecting the two interaction vertices (as shown in the latter figure), the scattering angle θ_2 can be determined. Subsequently, through double application of Equation 1, the complete kinematic reconstruction can be achieved [14, 15].

(a) Single scattering n-p.

(b) Double scattering n-p.

Figure 2: Neutron-proton scattering events: (a) single scattering and (b) double scattering.

The proton energy E_p is obtained by measuring the length of the proton track, known as the *range*. The range R of a heavy charged particle in matter is related to its energy E via the formula:

$$R(E) = \alpha E^p, \tag{2}$$

where α depends on the material, and p depends on the proton energy [14].

3. Geant4 Simulations

The detection concept proposed in this feasibility study has been supported through Monte Carlo simulations based on the Geant4 toolkit [16]. The scintillator cube, with dimensions of $60 \times 60 \times 60$ mm^3, was modeled using polyvinyltoluene, representative of the BC-408 material. Its properties were retrieved from the NIST database [17] and are available within the Geant4 material libraries under the name `G4_PLASTIC_SC_VINYLTOLUENE`. The material features a stoichiometric C/H ratio of 9/10, a density of 1.032 g/cm^3, and an ionization energy of 64.7 eV.

Simulations were performed using the standard Geant4 physics lists, which include suitable models for electromagnetic and hadronic interactions. Optical photon generation and transportation were enabled using the dedicated optical physics processes. According to the BC-408 datasheet [18], 10^4 optical photons were produced along the proton tracks for each MeV of energy deposition and then propagated within the plastic scintillator.

Neutrons were employed to study the scintillator response in terms of energy transfer to protons and the subsequent transport of these secondary particles. Neutron–proton and neutron–carbon interactions are concurrent reactions within the scintillator, and both interaction types were included in the analysis [12].

This work focuses primarily on simulations with neutrons as primary particles, with the aim of characterizing the scintillator response to ionization induced by secondary charged particles. Monoenergetic neutrons at 50 MeV were generated just outside the scintillator cube. Only elastic neutron-proton (n–p) scattering events were considered, ensuring that all ionization signals originated exclusively from recoil protons. Strategies based on Convolutional Neural Networks are also being investigated, with the goal of classifying the underlying interaction processes using only the scintillation light projections of the charged particles. The recoil protons have an energy that depends on the scattering angle, ranging from zero up to the full kinetic energy of the incident neutron.

As recoil protons traverse the plastic scintillator, the energy they deposit induces the production of optical photons. These photons are then collected by an optical system consisting of two plano-convex lenses with focal lengths of 75 mm and 60 mm, respectively, both with a diameter of approximately 50 mm. The lenses are arranged to form a *Ramsden eyepiece* [19]. The lens with the longer focal length is positioned closer to the sensor, as illustrated in Figure 3. The two lenses are separated by a distance of 1 mm. The distance between the scintillator and the lens system is $a = 80$ mm, while the distance between the lenses and the sensor is $b = 33$ mm. This configuration allows for a depth of field of approximately 20 mm and a field of view of $30 \times 30\,\text{mm}^2$, with a magnification of approximately 0.5. As a result, it is possible to project on the area of the sensor ($25 \times 25\,\text{mm}^2$), corresponding to a matrix of 512×512 pixels, where the full length of the proton tracks is clearly visible. The hits on the sensor cells due to the optical photons are finally recorded in the form of a two-dimensional histogram, ready for subsequent analysis.

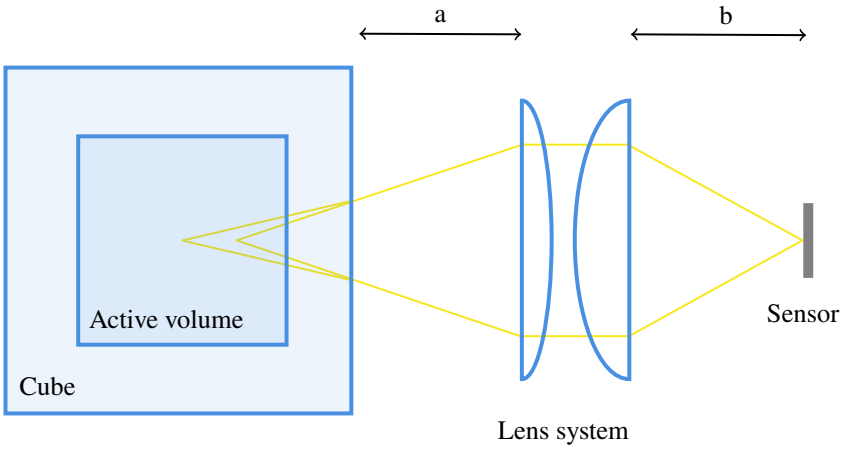

Figure 3: Sketch of a simple setup for the simulation of photon transport.

4. Track reconstruction

The aim of tracking reconstruction is to determine the energy and direction of incident neutrons by analyzing the projections of recoil proton tracks on the sensor, within the active volume of the scintillator. To achieve this, a combination of classical and machine learning-based techniques is employed.

4.1 Hough transform for direction

The Hough transform [20] is a technique for extracting geometric features from images. It is widely used in computer vision, particularly for detecting straight lines, by mapping points from image space to a parameter space where lines appear as peaks.

In Figure 4a, we observe the projection of the particle track with respect to the $+xy$-plane, which represents the input for the Hough transform. This image shows the raw trajectory data captured by the sensor. In Figure 4b, the corresponding Hough accumulator is displayed, where each point in the original image contributes a sinusoidal curve based on the parameterization. The accumulator

is filled by applying the Hough transform equation to the pixel coordinates of the track projection. Finally, in Figure 4c, the result of the Hough transform is shown. The peak in the accumulator, corresponding to the highest vote count (θ_p, ρ_p), provides the optimal parameterization which best defines the straight-line representation of the trajectory in the image space.

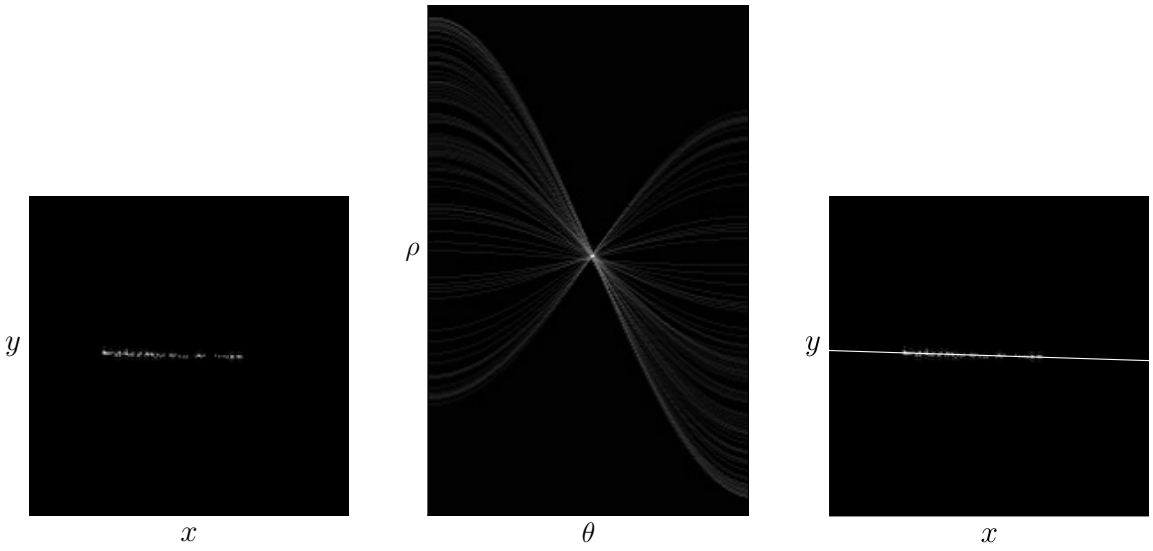

(a) Track projection. **(b)** Hough accumulator. **(c)** Hough transform result.

Figure 4: Hough transform steps: (**a**) +xy track projection on the sensor; (**b**) the accumulator is filled by applying the transformation on the previous projection; (**c**) the accumulator peak provides the best parametrization of the projection.

4.2 Momenta Method for Orientation

Following the determination of the track direction via the Hough transform, the track orientation is inferred by analyzing the energy loss profile of the proton in the scintillator, which follows the Bragg curve [21]. The procedure begins with the computation of the barycenter (x_b, y_b) of the track projection on the sensor, weighted by pixel grayscale values:

$$x_b = \frac{\sum_i w_i x_i}{\sum_i w_i}, \quad y_b = \frac{\sum_i w_i y_i}{\sum_i w_i}. \tag{3}$$

Coordinates are then translated so that the barycenter becomes the origin:

$$x_i \to x_i - x_b, \quad y_i \to y_i - y_b, \tag{4}$$

and the system is rotated by the angle θ_p, determined via the Hough transform, to align the major axis with the track:

$$\begin{pmatrix} x_i' \\ y_i' \end{pmatrix} = \begin{pmatrix} \cos\theta_p & -\sin\theta_p \\ \sin\theta_p & \cos\theta_p \end{pmatrix} \begin{pmatrix} x_i \\ y_i \end{pmatrix}. \tag{5}$$

The orientation is finally established by computing the skewness μ_3 of the grayscale distribution along the major axis:

$$\mu_3 = \frac{\sum_i w_i x_i'^3}{\sum_i w_i} = \frac{\sum_i w_i (x_i \cos\theta_p + y_i \sin\theta_p)^3}{\sum_i w_i}. \tag{6}$$

A negative skewness ($\mu_3 < 0$) confirms the orientation, while a positive skewness ($\mu_3 > 0$) indicates that the track direction must be corrected by setting $\theta_p \rightarrow \theta_p + \pi$. The method is illustrated in Figure 5.

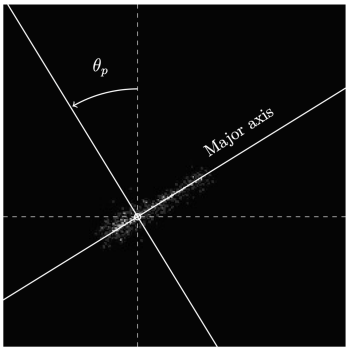

Figure 5: Representation of the steps in momenta analysis. First, the barycenter is identified, and the origin of the coordinate system is translated to the barycenter, then the axes are rotated by an angle θ_p.

4.3 Track Restoration and Length Estimation Using a U-Net Model

The optical system of the detector introduces aberrations that distort the reconstructed projected track length on the sensor. This effect reduces the precision of track length reconstruction and consequently affects the accuracy of the proton energy estimation. To mitigate these distortions, we employ a deep learning approach based on the U-Net architecture [22], which combines an encoder-decoder structure with skip connections to preserve both high-level contextual features and fine spatial details. The complete architecture, summarized in Table 1, consists of convolutional blocks with batch normalization (BN) and dropout layers for regularization. The encoder progressively downsamples the input, while the decoder reconstructs the original resolution.

During the training phase, the U-Net receives distorted track projections as input and learns to output corrected track images. The model is trained using simulated ground truth tracks—obtained from Geant4 tracking information without optical distortions—as targets, optimizing the Dice loss function. The model is trained using the Nadam optimizer [23] (learning rate 1×10^{-4}) and a Dice loss function [24], optimized for segmentation tasks. Training proceeds for up to 50 epochs with a batch size of 16, monitored by an *early stopping* callback that halts training if validation loss fails to improve over five consecutive epochs.

Model performance is evaluated using the mean absolute error (MAE) on a held-out test set. As shown in Figure 6, the training curves indicate convergence for both the loss and MAE metrics. The lower validation MAE compared to the training MAE is likely due to the effect of dropout regularization, which is active during training but disabled during validation, thereby acting as a strong regularizer.

Phase	Main Blocks	Output Shape	Param #
Input	Input Layer	(128, 128, 1)	0
Encoder	Conv2D + BN + Dropout (×2)	(128, 128, 64)	37,824
	MaxPooling2D	(64, 64, 64)	0
	Conv2D + BN + Dropout (×2)	(64, 64, 128)	221,952
	MaxPooling2D	(32, 32, 128)	0
	Conv2D + BN + Dropout (×2)	(32, 32, 256)	886,272
	MaxPooling2D	(16, 16, 256)	0
	Conv2D + BN + Dropout (×2)	(16, 16, 512)	3,539,968
	MaxPooling2D	(8, 8, 512)	0
	Conv2D + BN + Dropout (×2)	(8, 8, 1024)	14,157,824
Decoder	Conv2DTranspose + Concat (×4)	Variable	2,786,240
	Conv2D + BN + Dropout (×2 per block)	Variable	9,403,496
Output	Conv2D (1 filter)	(128, 128, 1)	65
Total			**31,054,145**

Table 1: U-Net architecture summary, detailing the encoder-decoder structure, layer dimensions, and parameter counts.

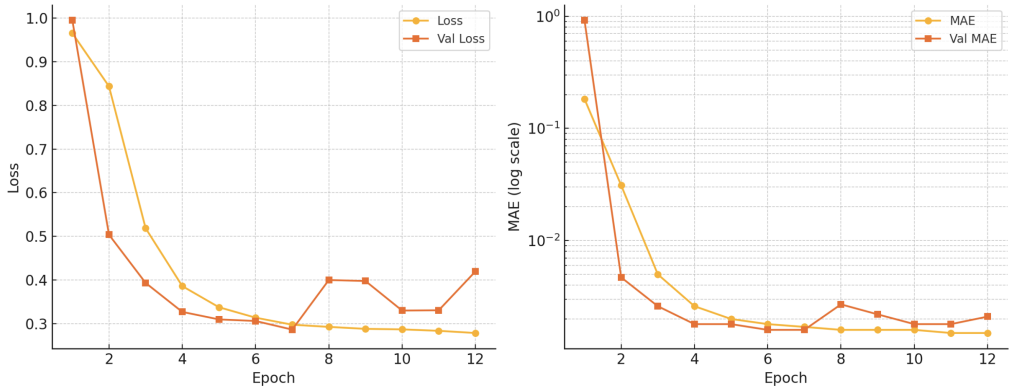

Figure 6: Training metrics: (left) loss progression and (right) validation MAE across epochs.

The restored track images enable precise length estimation by projecting the reconstructed tracks onto the sensor axes. A qualitative comparison between raw and U-Net-processed tracks is shown in Figure 7, highlighting the model effectiveness in correcting optical distortions.

5. Results

In this section, we summarize the preliminary results of reconstructing the three-dimensional direction of individual proton tracks from two projections, applying the Hough transform and moment analysis to determine the track direction θ_p. The reconstructed directions from the (xz)

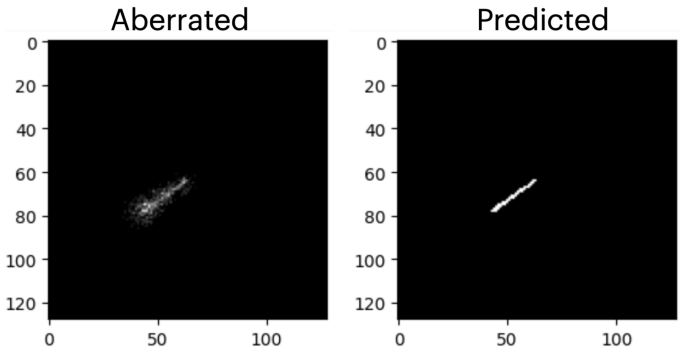

Figure 7: Track reconstruction results: original sensor image (left) versus U-Net-restored output (right).

and (xy) projections are denoted $\theta_p^{(xz)}$ and $\theta_p^{(xy)}$, and the corresponding track lengths are $\ell_{(xz)}$ and $\ell_{(xy)}$. To estimate the proton track x-component, we average the projections of the track lengths along the x-axis, yielding the 3D track vector as:

$$\vec{r} = \left(\frac{\ell_{(xz)} \cos\theta_p^{(xz)} + \ell_{(xy)} \cos\theta_p^{(xy)}}{2}, \ell_{(xy)} \sin\theta_p^{(xy)}, \ell_{(xz)} \sin\theta_p^{(xz)} \right), \tag{7}$$

with the normalized 3D track direction $\hat{r}_{reco} = \frac{\vec{r}}{\|\vec{r}\|}$.

The comparison with Monte Carlo truth in Figure 8 reveals that the resolution of the reconstructed $\cos\theta_{reco}$ is of 2%.

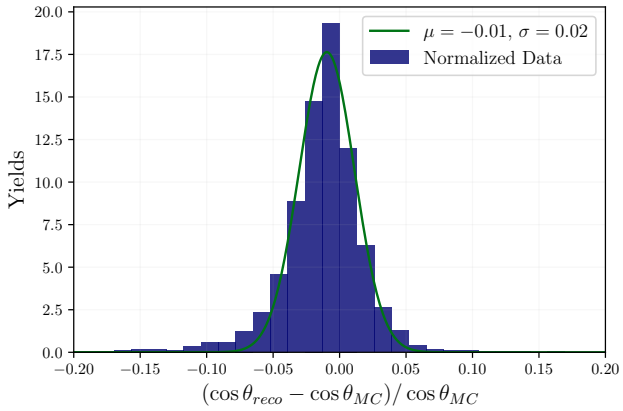

Figure 8: Normalized residuals between the reconstructed cosine of the angle $\cos\theta_{reco}$ and the Monte Carlo truth $\cos\theta_{MC}$ are presented; see the text for details.

Next, we compute the proton range using the track projections. The proton range, derived from the track projections, is calculated as:

$$R_{reco} = \sqrt{\left(\frac{\ell_x^{(xz)} + \ell_x^{(xy)}}{2} \right)^2 + \left(\ell_y^{(xy)} \right)^2 + \left(\ell_z^{(xz)} \right)^2}. \tag{8}$$

The resolution of the proton ranges is about 5%, as shown in Figure 9.

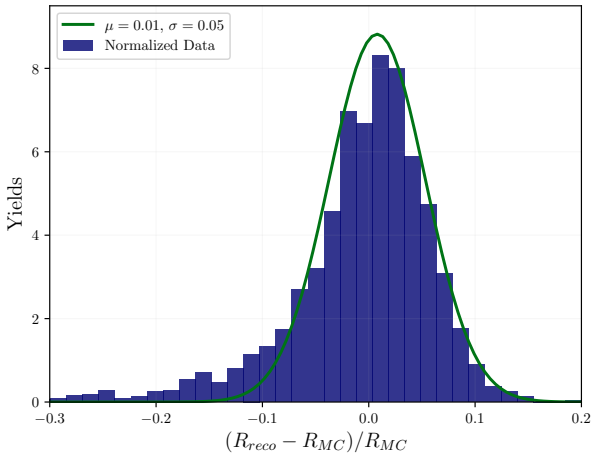

Figure 9: Normalized residuals between the reconstructed proton ranges (R_{reco}) and Monte Carlo truth (R_{MC}).

A different Monte Carlo dataset was used to establish an empirical relationship between proton range and energy (see Equation 2), yielding a two-parameter fit:

$$\alpha = (1.867 \pm 0.013) \cdot 10^{-2} \text{ mm/MeV}, \quad p = (1.803 \pm 0.002). \tag{9}$$

The relationship between the range and proton energy is shown in Figure 10, where the fitted empirical law is presented.

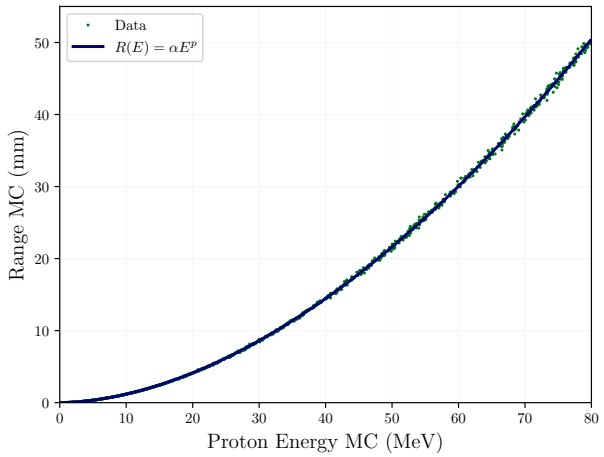

Figure 10: Relationship between range and proton energy. A two-parameter fit is performed to determine an empirical law that links proton range to its energy.

Finally, using these results, we reconstructed the neutron energy resolution through the proton track direction and range, achieving a 5% precision in the energy, as shown in Figure 11.

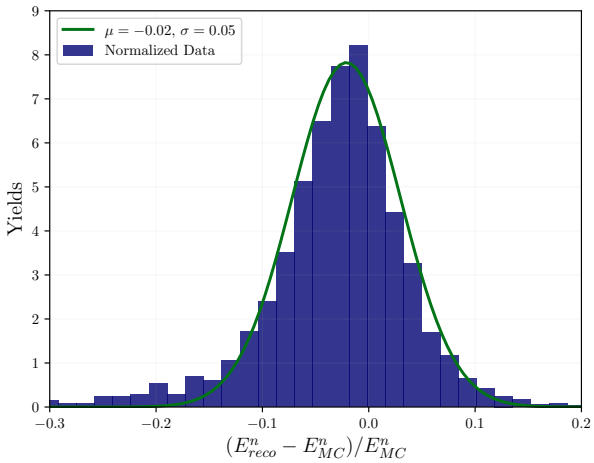

Figure 11: Normalized residuals between reconstructed and true neutron energy.

6. Conclusions

The primary goal of this work is to develop novel imaging techniques for neutron detection, specifically focusing on the RIPTIDE project, which tracks fast neutrons by visualizing proton recoil tracks via scintillation light.

The proposed track reconstruction method, based on stereoscopic imaging of proton-recoil tracks from Monte Carlo simulations, demonstrates promising results in accurately determining the 3D direction and orientation of tracks. When combined with deep learning algorithms for optical aberration correction, the method achieves a significant improvement in track length estimation, reducing reconstruction errors by 37.5% (from 8% to 5% resolution). This enhancement directly translates to more accurate proton energy determination and consequently improves neutron energy reconstruction.

Our study demonstrates the method's viability using a dataset of monoenergetic neutrons at 50 MeV, focusing on single scattering events. The achieved 5% resolution in neutron energy reconstruction validates the effectiveness of the combined approach employing both traditional computer vision techniques and deep learning-based image restoration. These results establish a strong foundation for future developments in fast neutron detection and spectroscopy.

References

[1] Hu, J., Liu, J., Zhang, Z. et al., *Recoil-proton track imaging as a new way for neutron spectrometry measurements*, *Sci Rep 8*, 13363 (2018).

[2] S. Valle et al., *The mondo project: A secondary neutron tracker detector for particle therapy*, *Nucl. Instrum. Meth.*, A845 (2017) 556.

[3] E. Gioscio et al., *Development of a novel neutron tracker for the characterisation of secondary neutrons emitted in particle therapy*, *Nucl. Instrum. Meth.*, A **958** (2020) 162862.

[4] G. Wangetal., *Optical Method Based on a Gaseous Scintillator for Neutron Energy Spectrum Measurements*, *J. Appl. Spectrosc.*, **87** (2020) 911.

[5] R. S. Miller, J. R. Macri, M. L. McConnell, J. M. Ryan, E. Flückigerand, L. Desorgher *Sontrac: An imaging spectrometer for mev neutrons*, *Nucl. Instrum. Meth.* A **505** (2003) 36.

[6] Z. Wang and C. L. Morris, *Tracking fast neutrons*, Nucl. Instrum. Meth. A **726** (2013) 145, arXiv:1210.8218.

[7] J. G. Mitchell et al., *Development of the Solar Neutron TRACking (SONTRAC) Concept*, PoS ICRC2021 (2021) 1250.

[8] G. A. de Nolfo et al., *Next-generation SOlar Neutron TRACking (SONTRAC) instrument*, Nucl. Instrum. Meth. A **1054** (2023) 168352.

[9] M. Marafini et al., *MONDO: a neutron tracker for particle therapy secondary emission characterisation*, Phys. Med. Biol. **62** (2017) 3299.

[10] A. Musumarra et al., *RIPTIDE: a novel recoil-proton track imaging detector for fast neutrons*, 2021 JINST **16** C12013,

[11] C. Massimi et al., *RIPTIDE — an innovative recoil-proton track imaging detector*, 2022 JINST **17** C09026.

[12] P. Console Camprini et al., *A proton-recoil track imaging system for fast neutrons: the RIPTIDE detector*, 2023 JINST **18** C01054.

[13] C. Pisanti et al., *Riptide: a proton-recoil track imaging detector for fast neutrons* 2024 JINST **19** C02074.

[14] J. F. Ziegler, M. D. Ziegler, J. P. Biersack, *SRIM – The stopping and range of ions in matter (2010)*, Nucl. Instrum. Meth. B **268** (2010) 1818–1823.

[15] G. F. Knoll, *Radiation Detection and Measurement*, 4th Edition, Wiley, 2010.

[16] S. Agostinelli et al., *GEANT4—a simulation toolkit*, Nucl. Instrum. Meth. A **506** (2003) 250–303.

[17] NIST, *Atomic Weights and Isotopic Compositions – Relative Atomic Masses*

[18] GENERAL PURPOSEEJ-200,EJ-204, EJ-208, EJ-212
https://eljentechnology.com/products/plastic-scintillators/ej-200-ej-204-ej-208-ej-212

[19] E. Hecht, *Optics*, 5th ed., Pearson, 2017. (Chapter on Compound Optical Systems)

[20] R. O. Duda and P. E. Hart, *Use of the Hough Transformation to Detect Lines and Curves in Pictures*, *Communications of the ACM*, vol. 15, no. 1, pp. 11–15, 1972.

[21] R. Bellazzini, F. Angelini, L. Baldini, A. Brez, E. Costa, G. D. Persio *et al.*, *Micropattern gas detector for x-ray polarimetry*, in *Polarimetry in Astronomy*, edited by S. Fineschi, vol. 4843, pp. 372–382, International Society for Optics and Photonics, SPIE, 2003.

[22] O. Ronneberger, P. Fischer, and T. Brox, *U-Net: Convolutional Networks for Biomedical Image Segmentation*, in *Proceedings of the International Conference on Medical Image Computing and Computer-Assisted Intervention (MICCAI)*, pp. 234–241, 2015.

[23] T. Dozat, *Incorporating Nesterov Momentum into Adam*, ICLR Workshop, 2016. Available at: https://openreview.net/forum?id=OM0jvwB8jIp57ZJjtNEZ

[24] F. Milletari, N. Navab, and S.-A. Ahmadi, *V-Net: Fully Convolutional Neural Networks for Volumetric Medical Image Segmentation*, in *Proc. 3DV 2016*, pp. 565–571, IEEE, 2016.